Original Article

Static roughness element effects on protuberance full-span wing at micro aerial vehicle application

Hossein Jabbari, Mohammad Hassan Djavareshkian[ORCID] and Ali Esmaeili

Abstract

Although the tubercle wings provide good maneuverability at post-stall conditions, the aerodynamic performance at pre-stall angles is threatened by forming a laminar separation bubble at the trough section of the tubercle wing; consequently, the flight endurance and range are reduced. In the present study, the idea of passive flow control is introduced by using the distribution of static roughness elements on a full-span wing with a sinusoidal leading edge. Initially, the effect of roughness element length, height, and its location are studied at a pre-stall angle (16-degree). Their effect on the laminar separation bubble and vortex shedding formed behind the wing are also investigated. The Reynolds number is assumed to be equal to 1.4×10^5 which is in the range of critical Reynolds number and matches to the micro aerial vehicles application. An improved hybrid model, improved delay detached eddy simulation IDDES, has been used to model the flow turbulence structure. In the extended transition region at low Reynolds numbers, the roughness bypassed the instability. Consequently, roughening the surface of the aerofoil increased the boundary layer's flow momentum, making it more resistible to adverse pressure gradients. By suppressing the bubble, the static roughness element led to pre-stall flow control, which saw an increase in lift coefficient, C_l, and a decrease in drag coefficient, C_d. The results have been demonstrated that the aerodynamic performance, c_l/c_d, has been improved approximately 22.7%, 38%, and 45% for $\alpha = 16°$, $\alpha = 12°$, and $\alpha = 8°$, respectively. The optimal arrangement of static roughness elements could decline the size of the vortices and strengthen the cores associated with them. This claim can be interpreted with the vortex shedding frequency.

Introduction

Inspiration from nature always contains new and practical ideas for researchers and scientists. In developing small aerial vehicles, birds and fishes have long been the focus of research, especially maneuverability. In recent years, attention to the physiological structure and morphology of a species of whale called Humpback has been shown special features among other aquatic animals, such as high agility and maneuverability features (rolling, loping, and turning). Despite their large size and rigid body, these maneuvres are performed when hunting prey due to their unique buoyancy fins. The structure of these fins is in the form of sinusoidal protuberances at the leading edge, as reported by Fish and Battel.[1] Furthermore, the combination of the protuberances and the fins' large aspect ratio gives this type of whale the ability to turn quickly.[2,3] Therefore, these observations and hypotheses led to more studies, experimental and numerical investigation, to understand the physics of flow in the presence of a sinusoidal leading edge. Miklosovic et al.[4,5] experimented with full-span and semi-span models in Reynolds close to the operating range of these whales ($Re \approx 3 \times 10^5$) in the wind tunnel. One of the most substantial results is the similarity of leading-edge protuberances' aerodynamic mechanisms on the finite and infinite wings resembling as seen at whale fins. Also, Weber et al.[6] and Van Nierop et al.[7] simulated the same models numerically and demonstrated a delay in the stall phenomenon in the leading-edge protuberance wing comparing to the baseline (traditional) wing. Therefore, this ability could

Faculty of Engineering, Department of Mechanics and Aerospace, Ferdowsi University of Mashhad, Iran

Corresponding author:
Mohammad Hassan Djavareshkian, Faculty of Engineering, Ferdowsi University of Mashhad, Vakilabad Ave, Mashhad 9177948974, Iran.
Email: javareshkian@um.ac.ir

maintain the lifting force and even increase the lift force at post-stall angles. Furthermore, Stein and Murray[8] considered leading-edge protuberances in the infinite models with the same wavelength and amplitude as measured at a real Humpback whale fin. However, they declared a reduction in lift force and an increase in drag force in the pre-stall angles. Further, Zhang et al.,[9] performed an experimental study on the sinusoidal edge infinite wing with a cross-section of NACA $63_4 − 021$ at $Re = 2.0 \times 10^5$ and compared their results with the values obtained from the Johari research.[10] All of them concluded that the leading-edge wavy model illustrated an aerodynamic performance loss in pre-stall situations, as reported by Hansen et al.,[11] too. They speculated that leading-edge tubercles produce counter-rotating vortexes, but they could not provide any reason for the effects of these changes. In the same investigation process, some researchers believe that the leading-edge tubercles' fundamental role may be a combination of several mechanisms.[12] Consequently, achievements such as diminishing the suction of flow in the peak zones, early occurrence of the transition, and even sub-harmonic behaviors have been reported.[13] Similar analyzes of the influence of the leading-edge protuberances on aerodynamic performance and flow characteristics at pre-and post-stall angles by other researchers with numerical simulations,[6,14–18] experimental approaches,[5,19–25] or both methods,[26–29] can be found. A common feature of previous studies, especially studies that used both experimental and numerical simulations, is performance decline and improvement at pre-and post-stall angles, respectively.

Numerical simulations can be beneficial in accomplishing more details of the flow field around infinite models. Therefore, many turbulence models were used to simulate and capture the existing phenomena accurately. For instance, the Spalart–Allmaras turbulence model is used by Dropkin et al.,[15] and the large eddy simulation model (LES) is used by Pérez-Torró and A. Skillen.[30,31] These turbulence models could not accurately estimate the exact location of the formed phenomena. Studies have also been performed to simulate the flow in the pre-stall status around the leading-edge protuberances; like Sousa and J. Camara,[16] Esmaeili et al.[32,33] simulated the flow around the wing with a sinusoidal edge modification for the various angle of attacks (AOAs) among 0° and 20° by using detached eddy simulation (DES) turbulence model. The DES turbulence model could predict the behavior and structure of streamwise vortices forming on the leading edge regions.

For the reasons stated earlier, a different distribution of velocity and flow patterns on the leading-edge protuberances can be expected. In this regard, Serson et al.,[13] following the study of Custodio et al.,[19] have reported asymmetry and non-periodicity behavior in the flow field. This phenomenon can be seen on the full-span wing for low aspect ratios and pre-stall angles with its specific patterns. Hence, considering the previous studies, it should be noted that one of the following two flow patterns appeared alternately on the troughs of the leading edge: (1) a typical movement of flow away from the trough or (2)

a general concentration of flows from neighboring peaks toward the trough.[26,34]

Considering the results and findings of background research, the spanwise distribution of flow has a significant effect on the aerodynamic performance of the sinusoidal leading-edge wing. An effective tool for applying these variations is to use surface roughness elements. So far, all research studies on the use of roughness elements mounted on traditional wings surface points to significant changes in flow behavior. These variations are such that a thin reverse flow zone is formed beneath the roughness particles' peaks. These portions indicate the effect of rotational areas behind each of the roughness elements on the intermittency coefficient of the flow near the wall. In other words, growth in turbulence kinetic energy can be seen in the shear layers for roughened cases. Another achievement of scientists is that the surface roughness accelerates the transition of the laminar-to-turbulent process. Such an event in the boundary layer leads to acceleration in the transition zone and, in a way, shortens the length of this zone.[35–38] Besides, it has been reported that excessive enhancement in roughness, both in height and density, increases the compression drag, intensifying the blockage impression. Increasing the surface of the elements can grow the local shear stress distribution. Compressive drag and friction drag influences are significantly reduced by enhancing the gap among the particles of the roughened part (density reduction).[36]

Investigating the flow physics on aerofoils with sinusoidal leading-edge modification can provide a new perspective on the flow control mechanisms, which is one of the current investigation's objectives. Since the flow distribution on the leading-edge protuberances has considerably influenced aerodynamic forces, especially in the appearance of laminar separation bubble (LSB), using flow control techniques can modify the flow field spreading. However, so far, less attention has been paid to this issue, and some have tried to change behavior and flow patterns by varying the number of protuberances on the leading edge. It should be noted that applying this method will not have the proper operational power to control the flow and dramatically increase the computational cost. Moreover, some past studies have employed active flow control methods that need more power and are not applicable in mico flyers. However, such a flow control method reduces the micro aerial vehicles (MAVs) and unmanned adrial vehicle (UAVs) flight endurance due to equipment and energy. Thus, in the current research, an efficient flow control manner called static roughness element is utilized to generate a uniform flow distribution, especially in spanwise direction without any additional equipment and energy. Also, this technique could influence on the LSB forming on the upper surface of the full-span wing. Furthermore, the size of the roughness element (length and width) and its rough height are mentioned, and its desirable features are obtained. By improving the flow field, these aerofoils' performance is on the agenda.

CFD approach

Wing models

To model the leading-edge protuberances, the NASA LS (1)-0417 cross-section was considered. According to background studies,[32] it was highly similar to the actual cross-section of the Humpback whale. Then, to create spanwise protuberances, the following analytical relation was used to create a sinusoidal leading edge on the wing

$$x = c + A \sin \left[2\pi \left(\frac{z}{\lambda} - \frac{\lambda}{2c} \right) \right] \quad (1)$$

where A and λ denote the amplitude and the wavelength of the protuberances, and x is the chordwise length, as illustrated in Figure 1. All baseline and modified wings exhibit the equivalent value of the mean chord $c = 232$ mm, hence sharing a common planform area if their aspect ratio (either $AR = 1.5$) is also the same. The values prescribed for the aforementioned geometrical parameters resulted from an earlier optimization study where a more significant set was analyzed,[16] viz. $A/c = 0.12$ and $\lambda/c = 0.5$ in non-dimensional form. The protuberances in the modified wings smoothly blend into the baseline profile, shown in Figure 1 by a dashed line.

The static roughness elements have been modeled using Fluent software features. When modeling a roughness element on an infinite wing surface, the grid density must be such that at least five cells can capture the roughness effects. Stripf et al.[39] revised the first correlation to model a turbine blade's wall roughness as follows

$$Re_{\theta tr} = \left[\frac{1}{Re_{\theta t}} + 0.0061 f_\Lambda \left(\frac{k}{\delta_t^*} - 0.01 \right)^{f_{Tu}} \right]^{-1} \quad (2)$$

where Λ indicates the density parameter utilized for a description of roughness, and f_{Tu} is a function expressing the effect of the free-stream turbulence. Stripf et al.[39] also added that this correlation was coherent when k/δ_t^* was between 0.01 and 3.[40] In addition to the above correlation, the flow over roughness wall based upon experiments conducted by Stripf et al.[39] was modified with the γ-Re transition model performed by Langtry and Menter.[41] The proposed correlation was defined as

$$Re_{\theta tr} = Re_{\theta t} \min \left[1; \frac{0.0554 + 1.005 \left(\frac{\theta_t}{k} \right)^{0.87}}{1.4629 + \left(\frac{\theta_t}{k} \right)^{0.87}} \right] \quad (3)$$
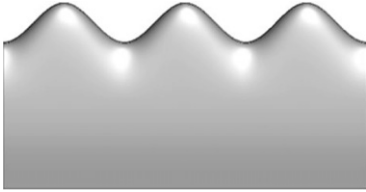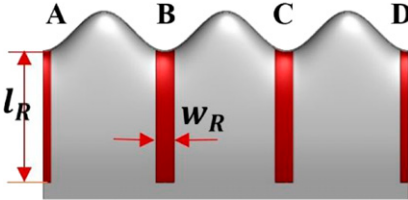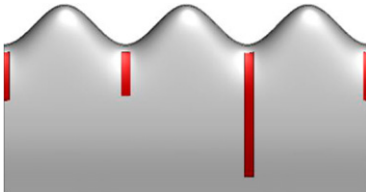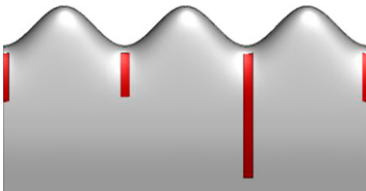
The simulations were accomplished by introducing the various geometries described in Table 1. The length of the roughness element (l_R), width (w_R), and height (h_R) were varied to compare their effects on the flow field. Various roughness elements are provided to find the best sample for flow control. Figure 1 defines the parameters for introducing the tubercle's full-span wing. A total of six different cases are presented in this paper, and they have been labeled as Cases 1 to 6.

The solver used in this investigation is commercial software Ansys Fluent ® version 19.2. The solution process is unsteady in the simulations, and the non-slip condition is considered for the desired geometry. It is
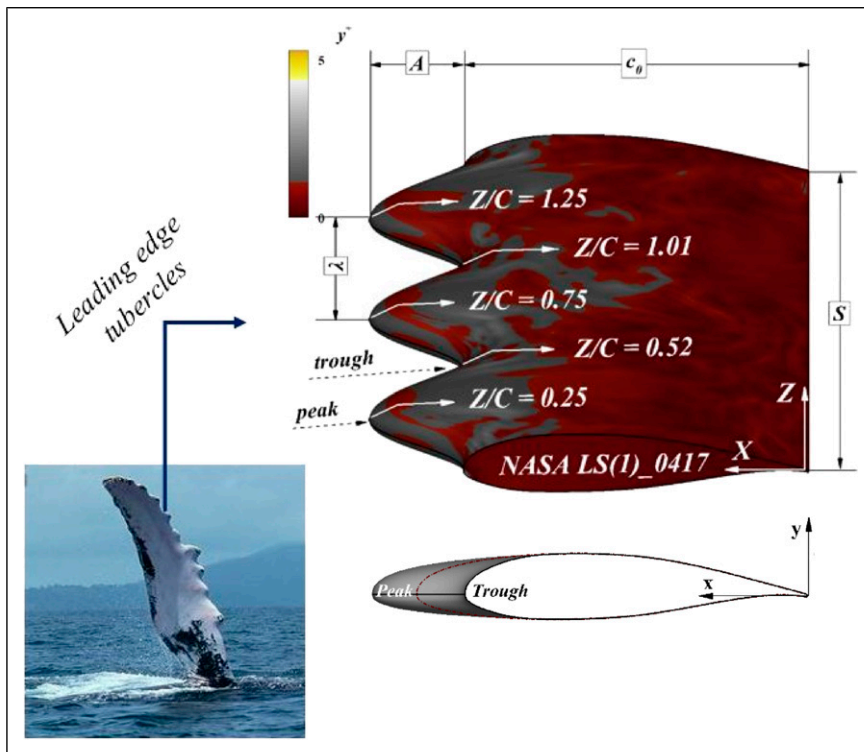
Figure 1. Three-dimensional view of the computational domain and boundary conditions and the spatial coordinate system.

Table 1. Dimensions of various cases considered in this research.

| Cases	Upper view	Passive control features (% c_{ref})		
		l_R	w_R	h_R
Case 1		0	0	0
Case 2		0	0	0
Case 3	A B C D	A 21 B 18.5 C 73.8 D 21	4 8 8 4	0.2
Case 4		A 21 B 18.5 C 73.8 D 21	2 4 4 2	0.2
Case 5		A 21 B 73.8 C 73.8 D 21	4 8 8 4	0.2
Case 6		A 21 B 18.5 C 73.8 D 21	2 4 4 2	0.6

worth mentioning that the roughnesses are located in chordwise rectangular elements in the troughs. Table 1 provides more details. One of the most critical Reynolds numbers in the low Reynolds range was chosen to scrutinize the effects of using roughness elements and approaching the flight regime of MAVs. The Reynolds number was 1.4×10^5 based on the middle of the chord length. In this case, the streamwise velocity is equal to 8.815 m/s.

Solving manner and governing equations

The numerical approach of this research uses the SIMPLE algorithm (a semi-implicit method for pressure-connected equations) and a second-order accuracy discretization for pressure. The quadratic interpolation solver (QUICK)[42] has been used to discretize the finite volume of conservation equations. However, temporal integration with implicit second-order accuracy is intended to reduce numerical stability constraints. Each simulation reported herein was conducted with a time step of 0.0025 s, though this value has been halved as a preliminary step to ensure independent time steps. The results showed that the time step is supposed to be of sufficient accuracy, and the results can be considered independent of the time step. Besides, according to Menter's proposal,[41,43] to adequately capture the laminar boundary layer and transition region, the value of y^+ had better be set to around 1.[44] In the present work, the value of y^+ varies in an appropriate
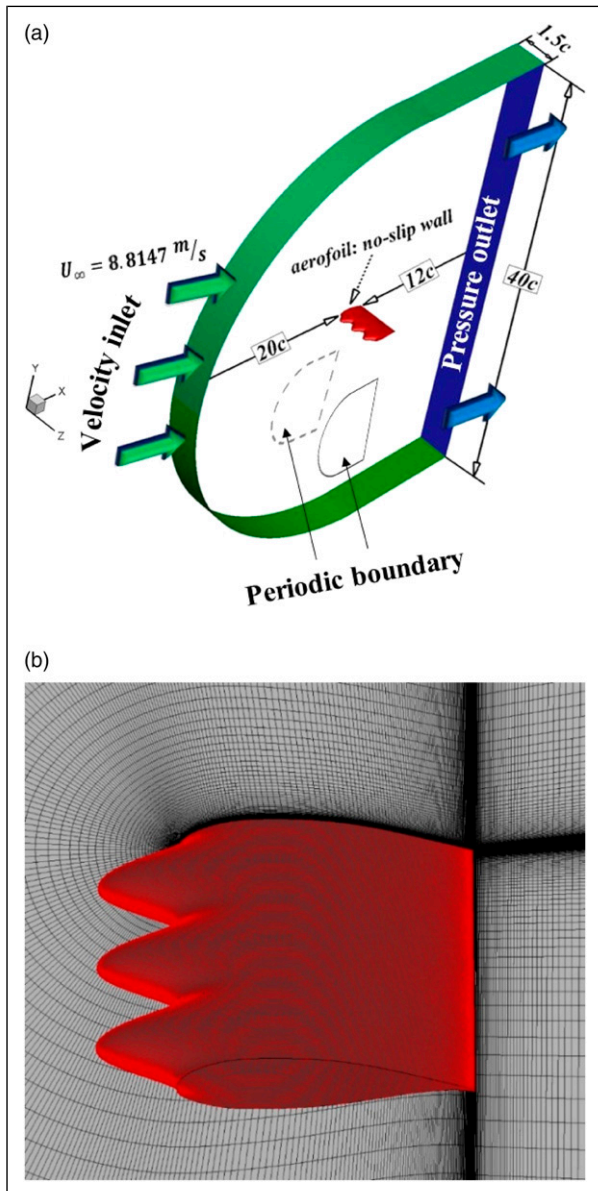
Figure 2. Geometrical definition of tubercle leading-edge wing models in (a) planform view and (b) side view (the dashed line indicates the baseline wing section).

range so that it corresponds to the requirements of the turbulence model.

Turbulence model

Among the numerous options available, the DES turbulence model was chosen in the leading study. Hybrid models with a common surface also have several different methods; the most widely used is the DES method. Previous researchers have called this model turbulence "DES" because it uses Reynolds-averaged Navier-Stokes (RANS) methods in regions adjacent to wall and the LES method for modeling vortices separated from the boundary layer and far from the wall portions. The connection between the RANS and LES zones is switched on automatically. In recent years, it is noteworthy that modifications were made to address
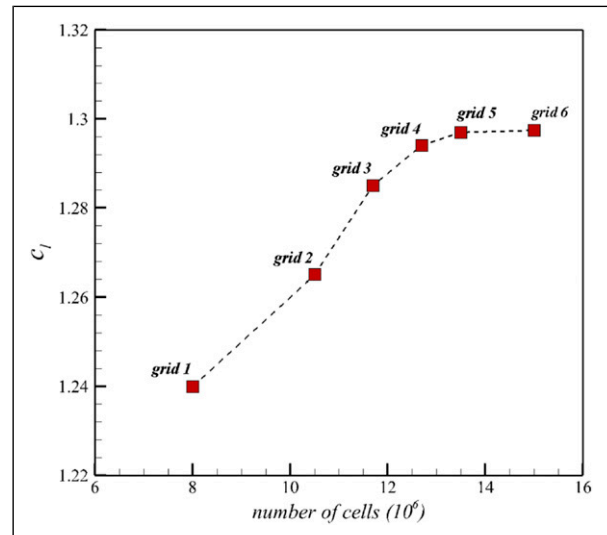
Figure 3. Mesh convergence.

some of the shortcomings in the model, which led to the introduction of DDES and improved delay detached eddy simulation (IDDES) models. In this simulation, the IDDES version has been used. Further details of this turbulence model are discussed in detail in Refs. 45–48.

It is worth noting that most simulations also take more than 40 s to solve to achieve a proper convergence. Also, averaging was performed from 400 instantaneous states to calculate the time-averaged results. These numbers cover approximately 10 s after convergence.

Meshing, boundary conditions, and grid independence

The computational domain is generated using the hybrid C-H topology, as exhibited in Figure 2. The velocity inlet boundaries were set at a distance of approximately 20c around the wings. The most beneficial fundamental domain has been picked to establish a logical relationship between computation and solution quality. The outlet pressure boundary condition is used at the output boundary, which is imposed at a distance of 12c downstream of the trailing edge of the wings, and no-slip conditions were applied at all solid wall surfaces. Measuring the computational domain is based on a balance between computational effort and the solution quality, which is highly compatible with Ref. 32.

Generating a structured mesh for such complex geometries involving curved surfaces was challenging, especially for the wings with leading-edge protuberances. However, the alternative use of an unstructured mesh has proven to be a less accurate option when wall boundary layers must be resolved. A way out of the dilemma was nevertheless found, which consisted of splitting the computational domain into four (more minor) volumes and providing better control over the density of

a structured mesh. The first two volumes were generated for the C-contour encircling the wings, from upstream to downstream, where mesh cells were adequately clustered near the solid walls, using a geometric expansion, to resolve the viscous boundary layers.[49,50] Such a rule has been applied in the present study, especially in roughened cases with high obsession. Besides, to ensure the meshing quality, the curvature and dimensionality of the cells were controlled. The minimum critical values of these parameters are obtained in the whole computational field. Therefore, to prevent the formation of cells with high skewness, the shortest possible distance was considered for the first cell near the walls.

The value of the lift coefficient at $AOA = 16°$ for six grids with different cell counts was examined to ensure the correctness of the results and its independence from the number of cells. Figure 3 shows the lift coefficient variations curve in terms of the number of cells in the mesh. According to the curve trend, it is clear that grid 5 is the most appropriate in terms of accuracy and volume of calculations.

Result and discussion

Flow control techniques on the wings have always been of interest to researchers because it saves energy and recovers the flight efficiency. The background investigation has demonstrated that protuberances at the wing's leading edge could benefit post-stall angles. However, the aerodynamic performance had reduced significantly in pre-stall angles. Although increasing attack angles in MAVs is vital for flight maneuvrability, reducing aerodynamic performance in pre-stall angles could sharply decrease the endurance and flight time. On the other hand, the performance loss is due to a LSB on the trough section of the tubercle leading edge wing. Therefore, the usage of roughness elements (one of the most efficient methods) to prevent the formation of undesirable phenomenon of laminar separated bubbles is considered in this research, and its effect of limiting the separation area has motivated. Furthermore, frequency analyses of various roughness elements have been discussed in this part. Initially, the roughness element, its length, and height have been investigated at an attack angle of 16° on a full-span sinusoidal leading-edge wing at $Re = 1.4 \times 10^5$. Due to the growth and turbulence of the boundary layer, increasing viscosity influence and attendance of a cycle of hysteresis around the stall angle enhances the complexity of the problem. Under these conditions, the lift coefficient for the baseline model approaches its maximum value and experiences shaky conditions. By contrast, for leading-edge protuberances aerofoil, the lift coefficient slope in the pre-stall is significantly lower than in the baseline model. The presence of these protuberances produces chordwise vortices, which are thicker than the boundary layer. Such situations lead to adequate mixing of the flow.[26] This mechanism delays the stall. On the other hand, protuberances and induced flows from the peak-to-trough enhance the drag coefficient in the pre-stall. One of the
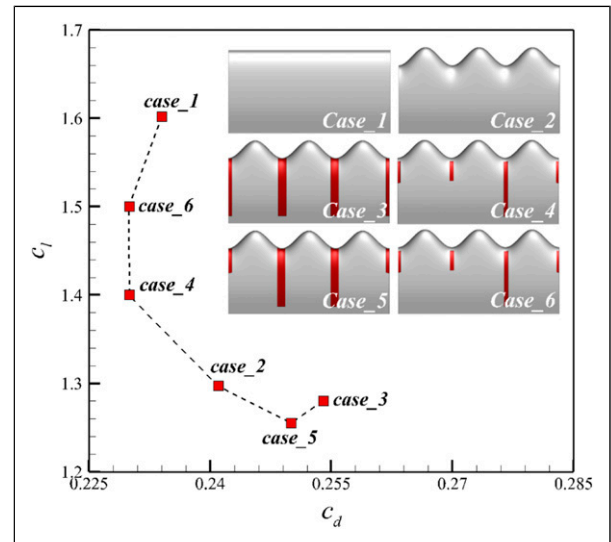

Figure 4. Polar diagram change rate for Cases 1 to 6 at AOA = 16°.

factors influencing this unpleasant event is the LSB phenomenon, which is significantly affected by environmental and local conditions.

In line with the expressed content, rectangle roughness elements with different characteristics are embedded in troughs because most changes occur in those portions. The influence of roughness on the aerodynamic coefficients of each case is presented in the form of a polar diagram (Figure 4).

Even though tubercle wings provide good maneuvrability at post-stall angles, the LSBs in the trough portion of these wings prevent proper aerodynamic performance at the pre-stall regime. By comparing the aerodynamic coefficients of Case 1 and Case 2, it can be verified this claim. According to Figure 4, the lift coefficient of Case 2 reduced by about 19.78% compared to that of Case 1, while its drag coefficient increased by about 3%. The static roughness elements are inefficient if they are in unfavorable dimensions and positions. For instance, Case 3 and Case 5 failed to improve aerodynamic performance and showed significant decreases compared to their original state (Case 1). As revealed in Figure 4, the lift coefficient of Case 3 and Case 5 augmented by 1.37% and 3.23% compared to that of Case 2, respectively.

Additionally, such an arrangement of roughness elements increases frictional drag. Therefore, the drag coefficients of Case 3 and Case 5 are ~5.4% lower than that of Case 2. Alternatively, if the position and dimensions of static roughness elements are appropriate, then aerodynamic performance can be improved. Both Case 4 and Case 6 exhibit such an event, as illustrated in Figure 4. In addition to increasing the lift coefficient in these models (approximately, 7.94% and 15.65% compared to Case 2, respectively), the drag coefficient has also reduced by around 4.6% compared to Case 2. It is worth noting that according to Table 1, the only difference between Case 4 and Case 6 is the height of the roughness element.
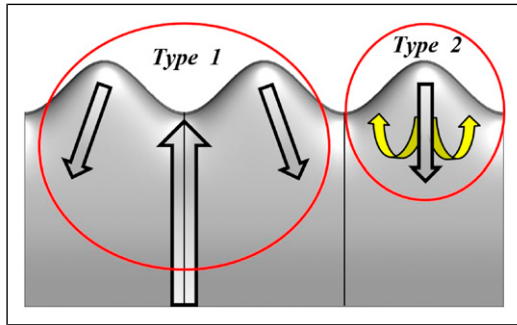
Figure 5. Typical aperiodic flow patterns on the modified airfoil.

Nevertheless, the pressure gradient growth from the neighboring peaks to the troughs and the disruption of the flow pattern were the factors that did not improve the performance of this sample. Conclusions imply a drop of about 26.67% in the performance of Case 5 compared to Case 2. To minimize the performance difference between the baseline aerofoil and sinusoidal leading edge, an attempt was made to increase the roughness height. By selecting the arrangement of the elements considered for Case 6 and increasing the roughness height to about 0.6 c, the most optimal state was obtained, the tubercle's infinite wing in Figure 5. In other words, by raising the height of the roughness elements (to a certain extent), the turbulent kinetic energy in the shear layers increases and accelerates the laminar-to-turbulent transfer process. Indeed, the boundary layer is influenced by roughness elements, leading to acceleration in the transition zone and shortening the length of this area.[36–38]

The non-coplanarity of the leading edge of models 2 to 6 creates a thoroughly three-dimensional flow that is particularly complex compared to the baseline aerofoils. This flow group generally induces some lateral velocity to the central areas chordwise while passing through their path. Following the contents expressed, the flow passing has a relatively strong lateral velocity component that deviates when it reaches the trough region and acts as a small AOA. This deflected flow interacts with streamwise flows, focusing on the midpoints behind the troughs, eventually leading to a bi-periodic distribution of flows in those areas. Due to mentioned factors, the amount of pressure distribution creates low-pressure portions on the troughs and leads to complex and asymmetric flow patterns in pre-stall conditions. These analyses are highly consistent with experimental results.[15,20,27,51] Therefore, two flow patterns are formed in different spanwise positions. Figure 5 shows an overview of them.

1. For Type 1, a large region of leading-edge separation is formed at the protuberance trough. The attached flows originated from neighboring peaks have a relatively strong lateral velocity component, deviating from the trough segment.
2. For Type 2, an attached flow on the protuberance peak in the middle keeps nearly straight toward downstream, while the attached flows from neighboring

peaks concentrate toward the mid-peak. Consequently, small reversed flows occur at the troughs.

The numerical simulations for Cases 2 to 6 illustrate the variation in flow behavior with changes in the properties of the roughness element at different spanwise positions. Figure 6 exhibits the pressure coefficient distribution and streamlines in the suction side of the infinite wings for Cases 2 to 6. According to this figure, other flow patterns other than the structure of the first and second types can be pointed to in some cases. However, the first and second patterns are an integral part of this configuration. When asymmetric roughness elements were used, a very weak negative compression coefficient occurred in the first type flow and a relatively strong value for the second type. It is noteworthy that the difference in pressure coefficient is more evident in the trough portions, while the pressure coefficient in the peaks has a moderate level.

On the other hand, the periodic pattern flow occurs using symmetric and quasi-symmetric roughness elements on the sinusoidal leading-edge (Cases 3 and 5, respectively). In these cases, due to the arrangement distortion of the first and second types of flow patterns, a reduction in c_l/c_d happens compared to other samples. In fact, in different positions, such as the two central areas of the aerofoil, the phenomenon of LSB and intense separations befall (Figure 6 confirms such a claim). Such a flow distribution would not be desirable.

In these conditions (pre-stall), if the roughness elements are not used, local adverse pressure gradient increases will appear in different situations. This event is an essential factor in reducing the lifting force and enhancing the drag compared to the baseline aerofoil. The bi-periodic features and structures of the flow by the arrows are exhibited in Figure 6.

To complete the previous section, the contour of $|V|^2$ $[m^2/s^2]$ was considered on the offset surface at $y/c_{ref} = 4.3 \times 10^{-4}$. Figure 7 manifests the changes $|V|^2$ on the suction side of two cases 2 and 6. This figure reflects the momentum magnitude in the boundary layer. Compared with Case 2, a higher momentum can be observed around the protuberance peak of Case 6. This phenomenon implies that the boundary layer is re-energized by the streamwise vortices produced by the protuberances due to roughness elements in those regions. The near-wall momentum around the protuberance valley is weakened. Failure to flow control will lead to an earlier leading-edge separation. The flow condition past leading-edge protuberances at the pre-stall will be such that one side experiences the stall condition and the other in the non-stalled state.[22] In this study, where $Re = 1.4 \times 10^{5}$ and the critical AOA is 16°, one-sided stall phenomenon and non-periodic pattern occur. As pointed out in Refs.6 and 52, attached flow can be observed on the peak of the single protuberance, which compartmentalizes the flow field and limits the spanwise extension of the stalled region. Also, in these two samples, local separations leading-edge occurs at two of the trough sections.
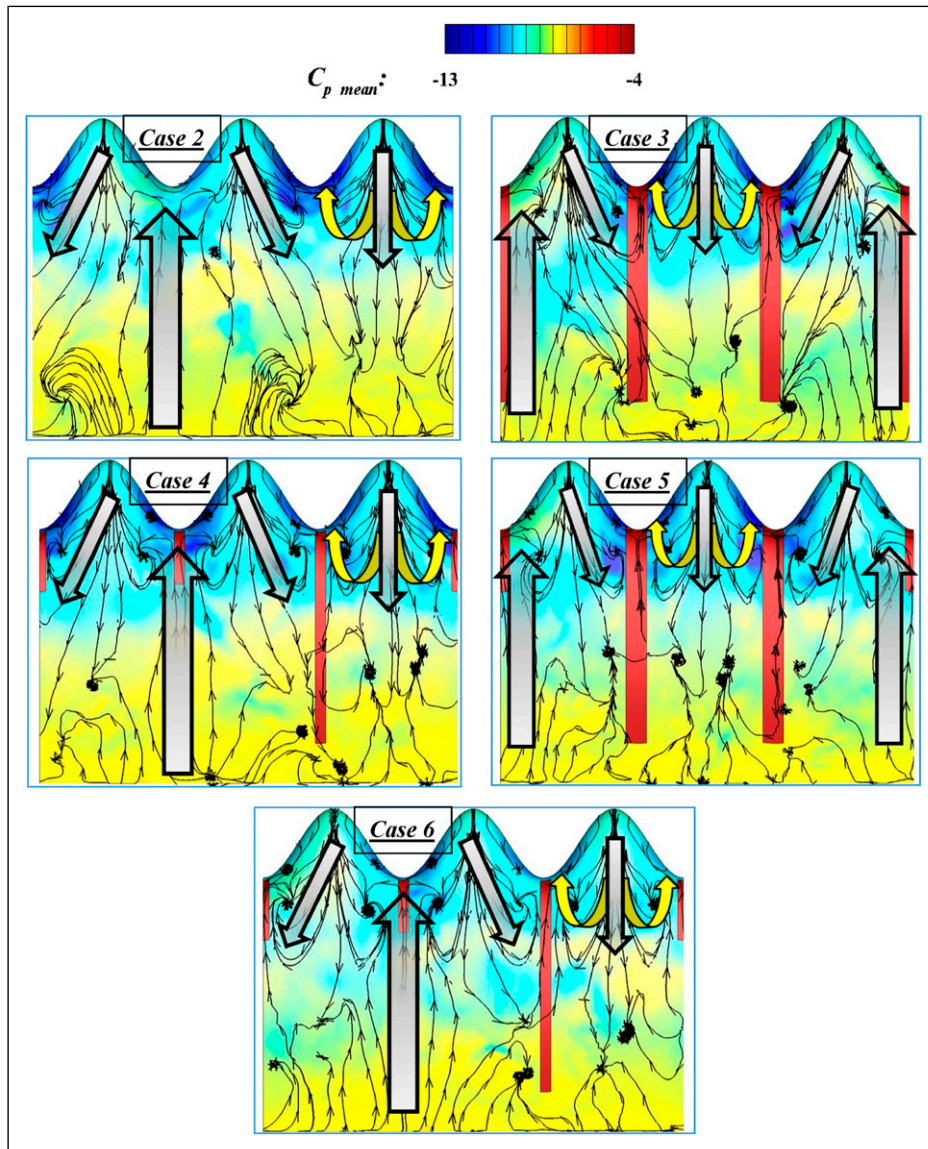
Figure 6. Pattern and structure of flow with the time-averaged pressure coefficient distribution on the suction side of Cases 2 to 6.

Frequently, the slender momentum-enhanced regions, which extend to around the trailing edge, compart the suction side into different regions, with the alternate occurrence of divergent-type and convergent-type compartmentalization. For the divergent-type compartmentalization, the spanwise extension of the leading-edge separation region is limited. For the convergent-type compartmentalization, the near-wall momentums on the suction side are replenished, thus avoiding the stall in this area. The presence of roughness elements makes divergent patterns convergent.

Time-averaged characteristics

This section was written and compiled to compare the time-averaged characteristics around the various cases in Table 1.

Pressure distribution. In Figure 8, a visual representation of the general comparison between the changes in the

behavior of the time-averaged pressure coefficient curve for Case 2 can be seen. This comparison is presented separately for the five vital parts of the aerofoil suction and pressure sides. These segments include three peaks and two troughs. In each of these curves, a uniform region in the time-averaged pressure distribution is evident. This area can be affected by the separation boundary layer on the suction side, which occurred with a separated shear layer. The distribution of the mean pressure coefficient for different z/c_{ref} takes on various patterns. Different local and environmental situations prevail in those areas. As displayed in Figure 8, the flow separation at $z/c_{ref} = 0.52$ begins near the leading edge and surrounds almost the entire length of the chord. However, at $z/c_{ref} = 1.01$, the flow separation occurs by delay compared to the previous state. Thus, it creates a region with an almost constant pressure level in the range $0.03 < x/c_{ref} \leq 0.09$. The separated flow returns to the aerofoil surface after a distance of approximately $l_{LSB}/c_{ref} = 0.26$. After this zone, which
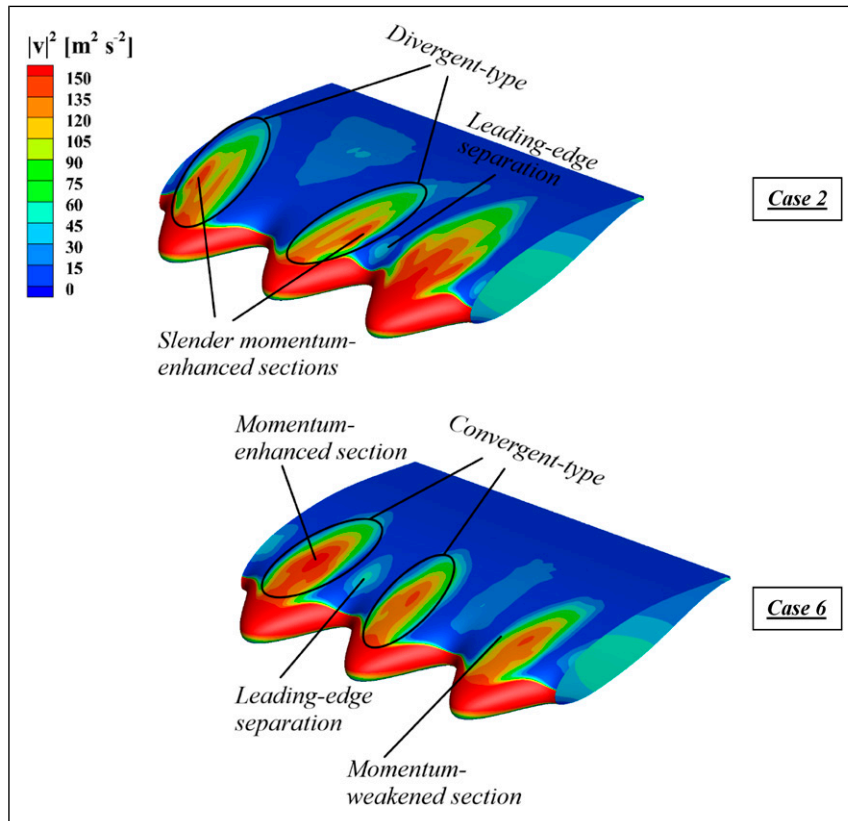
Figure 7. The time-average $|V|^2$ on the near-wall surface $y/c_{ref} = 4.3 \times 10^{-4}$ offset from the aerofoil.
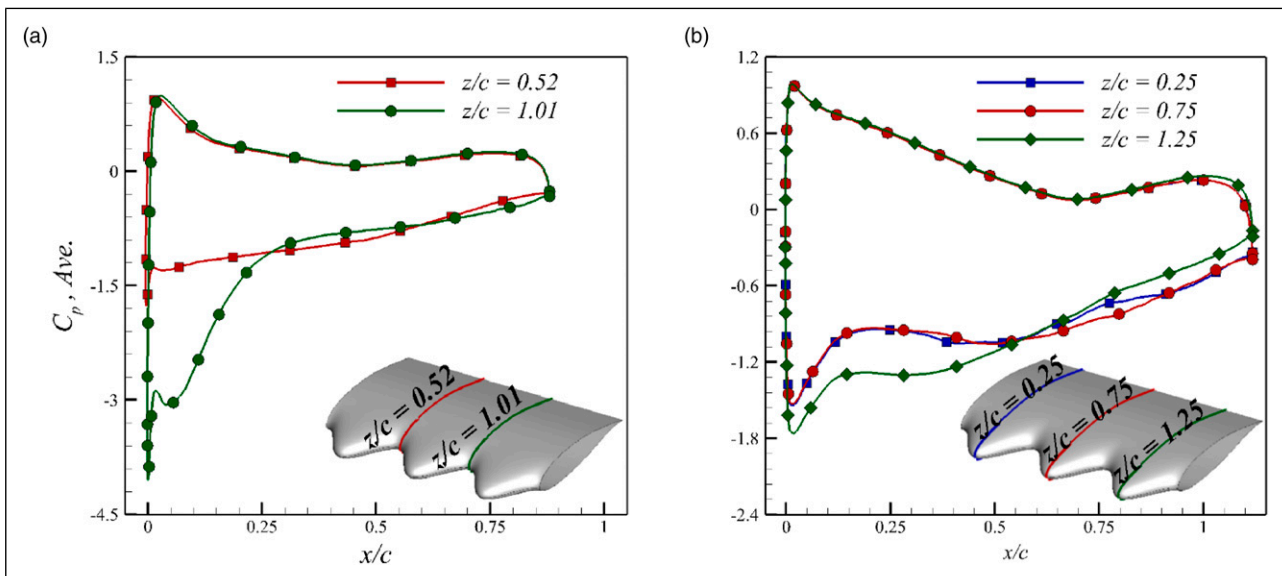

Figure 8. Comparison of changes in the time-average pressure coefficient of the infinite wing of Case 2 for (a) two troughs with $z/c_{ref} = 0.52$, 1.01 and (b) three peaks with the characteristic $z/c_{ref} = 0.25$, 0.75, and 1.25.

is accompanied by pressure recovery and return of flow to the surface, the tendency to decrease in pressure continues. Then a laminar-to-turbulent transition occurs downstream. Indeed, the momentum enters the area separated from the upper layers and causes the flow to re-attach the surface. It is noteworthy that the re-attachment flow leads to a significant pressure increase on the suction side of the

aerofoil. As the length of the bubble rises, the slope of the stagnation pressure curve increases. This event causes a thickening of the wings at the point of bubble formation. Variations in the time average pressure coefficient from the stagnation point to the trailing edge indicate the flow deviation from the peaks to the troughs. Such a process can exert a significant pressure change in the streamwise
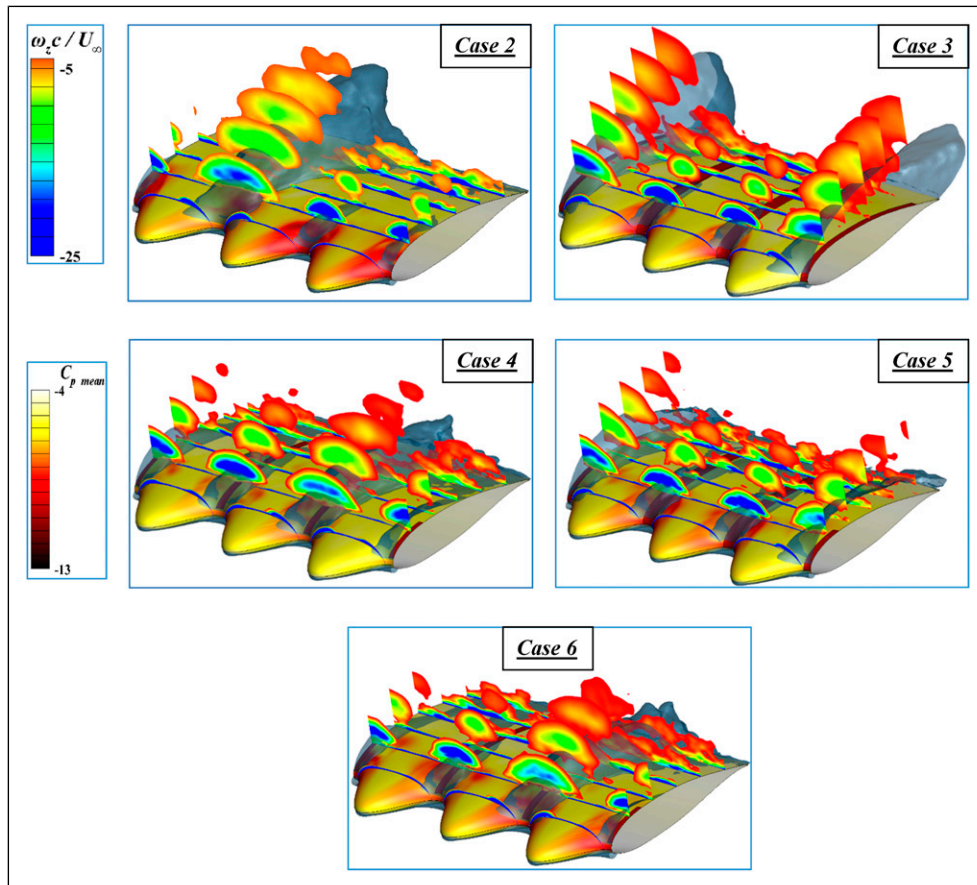
Figure 9. Time-average vorticity distribution, ISO-surface ($V_x = 0$), and time-averaged pressure coefficient on full-span suction side for sample 2 to 6 at AOA = 16°.

direction. Hence, it can be inferred that the peaks, which also cause a sudden pressure drop behind the troughs, play an essential role in gradually reducing the time-average pressure on their slope. Another noteworthy point in this figure is the distinction between the stagnation pressure for $z/c_{ref} = 0.25$ and 0.75 with $z/c_{ref} = 1.25$. The peaks at $z/c_{ref} = 0.25$ and 0.75 are strongly influenced by the low-pressure zone and significant separation in the valley between them. On the other hand, the peak at $z/c_{ref} = 1.25$ is enclosed between two valleys with relatively small bubbles. As a result, these conditions lead to a further drop in stagnation pressure at the two peaks $z/c_{ref} = 0.25$ and 0.75.

Vortices on wing. Figure 9 manifests more details of the field and flow structure around each of the samples. The dimensionless vorticity distribution is shown in this figure for various chordwise positions (according to equation (2)). Also, to better describe the Vortex core, the iOS-surface with characteristic $V_x = 0$ was applied on the suction side of the cases. To properly appreciate the flow physics, the models' skin also depicts the time average pressure coefficient distribution

$$\omega_z^* = \frac{\omega_z \bar{c}}{V_\infty} = \left(\frac{\partial V_y}{\partial x} - \frac{\partial V_x}{\partial y} \right) \frac{\bar{c}}{V_\infty} \qquad (4)$$

A couple of counter-rotating vortices are formed on the slope of each protuberance, as indicated in Figure 9. In other words, the secondary flows of Prentle's first kind are the main reason for these vortices.[28] These vortices play an influential role in delaying separation if they have sufficient power. These vortices extend the perturbation in the boundary layer, so leading to increased momentum and delaying separation.

The results show a lack of rotational flow formation on the peaks up to mid-chord length. The flow in these regions serves as a low AOA, and due to the proximity of the center of the vortices to the surface, they interfere with the boundary layer. In contrast, the flow in trough portions rotates due to the growth and amplification of the pressure gradient and rotation of the shear layers. Thus, the increase and expansion of vortices in the direction perpendicular to the surface can be seen. As the flow develops downstream, particularly past the protuberance, the peak magnitude of the initial vortex reductions in the streamwise direction while the region of vorticity expands in the area. The counter-rotating streamwise vortices separate from the surface at a specific chordwise location. Gradually, caused by interactions and mergers of the downstream vortices, the transverse growth of the vortices also appears. The intensity of the existing pressure gradients and severe separations is significantly reduced by distributing the roughness elements. This action lessens the nutrition of
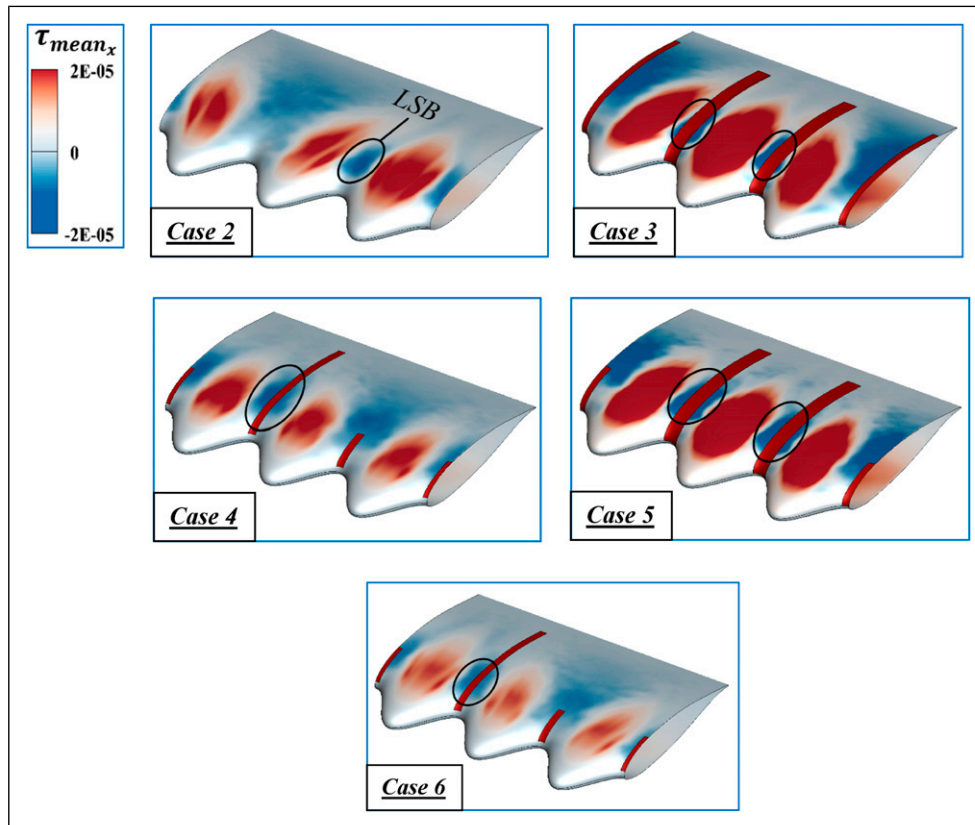
Figure 10. Time-average shear stress distribution on full-span suction side for sample 2 to 6 at AOA = 16°.

the vortices while weakening the rotation of the shear layers. Figure 9 is a visual description of this analysis.

The effect of the streamwise vortices can be estimated by Prandtl's lifting line theory,[53,54] which was initially proposed to consider the effect of tip vortices of finite wings. Under the influence of the counter-rotating streamwise vortices, a localized downwash velocity component will occur at each peak portion of the airfoil. Reciprocally, an upwash velocity occurs at each trough section. According to Prandtl's lifting-line theory(LLT), the downwash velocity will decline in the effective local AOA at this spanwise position. The upwash velocity will increase the effective local AOA. Therefore, it can be expected that the trough section will reach the stall angle earlier than other regions when the geometric AOA exceeds some critical amount.

Shear flow distribution. The magnitude of shear stress exhibits a distinct role in terms of the effect of skin friction over the surface. The presence of protuberances at the leading edge automatically causes extensive variations in shear flow conventional patterns on the suction side. The protuberances at the leading edge generate shear stress due to longitudinal flows and produce stresses influenced by lateral flows. Following the development of leading-edge vortices and counter-rotating vortices, the pressure drop in the toughs is noticeable. The combination of these flows with the existing vortices causes stress changes, especially in the trough sections.

Figure 10 illustrates the time-average shear stress on the suction side of Cases 2 to 6. In general, the magnitude of wall shear stress at the peaks is significantly less than

the stress distribution at the leading edge of the baseline wing. In other words, in all sinusoidal leading-edge cases, the shear stress declines with a relatively steep slope. The outputs of Figure 10 are separation and separation bubbles, which are demonstrated in this figure with zero stress and a closed black curve, respectively. The attendance of roughness elements with various dimensions changes the stress distribution remarkably. For example, in Case 2 and at $z/c = 1.01$, the decreasing trend of shear stress continues up to around 0.1 c. After passing this gradual process, the amount of stress due to flow separation reveals a constant zero value.

Furthermore, a couple of points indicate negative stress, which is affected by reversible flows. In Case 2, at z/c, stress is reduced to around 0.2 c and close to zero behind the trough. This region is where the separation bubble forms, and due to the reversible flows, the stress values decrease below zero. On the other hand, shear stress enhances by re-attaching the flow at the end of the formed LSB. Such a pattern is strongly consistent with other previous investigations.[52,55]

According to Figure 10, the sharp varieties in the stress distribution in the downstream areas of the peaks can be acknowledged. The red spots on the slopes of the peaks indicate positive and increasing values. This event presents an increase in velocity gradient and leads to grown shear stress on the suction side of these models. On the other hand, the influence of roughness elements on the amount of stress and shear forces is notable. As can be seen, the roughness is associated with an increase in the stress distribution downstream of each element.

Instantaneous characteristics

In Figure 11 is plotted the time history of lift coefficient fluctuations for Case 6. Its process is identical to Cases 2 to 5. The most critical instants in the LSB evolution in proportion to time are labeled in this figure. A noteworthy point in Figure 11 is a couple of oscillations in the lift coefficient (at the stage of shedding and development of vortices). Such behavior is affected by LSBs and flow separation that begins to form from the leading edge. In parallel with Figure 11, to better comprehend the flow physics in Case 6, the instantaneous pressure coefficient curves for points A, B, C, and D are presented in Figures 12 and 13.

As mentioned earlier, the considerable segments on this full-span wing are divided into three peaks and two troughs. As shown in Figure 9, no particular phenomenon occurs on the peaks, but they play an efficient role in forming phenomena and flow structure.[52] Therefore, the instantaneous pressure coefficient changes on the peaks at $z/c_{ref} = 0.25$, 0.75, and 1.25 are related to the lateral flows or their dominance and defeat relative to the streamwise component. According to the previous section, such variations lead to the formation and non-formation of low-pressure regions and flow deviation. In other words, these low-pressure regions are prone to flow attraction, which changes the flow patterns, as in Figure 12.

In contrast, significant issues occur in the valley portions. Indeed, each trough is affected by induced flows from its two neighboring peaks. These sections can be the site of the LSBs or flow separation. To investigate the physics of flow in the trough portions, further Figure 13 exhibits the instantaneous pressure coefficient curve at different times. Figure 14 is also presented as a supplement in the form of instantaneous velocity distribution.

At $t_A = 15.2\ cs$, according to the flow behavior in the pressure coefficient curve and the corresponding velocity distribution structure in Figure 14, this time belongs to the instant of LSB formation at $z/c_{ref} = 0.52$. Simultaneously, phenomena such as flow attachment to the surface, the tendency to positive pressure gradients (Figure 13), and separation from the surface (Figure 14) are also evident, at $z/c_{ref} = 1.01$. In these situations, according to Figure 11, the maximum lift coefficient is obtained. Over time at the instant $16\ cs$, the pressure drop in the valley areas reaches such a point that the LSBs are fully formed and show a tendency to grow. On the other hand, at this instant, with the emergence of reciprocating flows, the beginning of separation is imminent. It is caused by continuous induce flows that originate from the peaks. Consequently, a relatively significant drop in the lift coefficient appears. Figure 11 can be interpreted. As a result, at instant B relative to A, a drop of approximately 13.8% occurs.

The formation of separation bubbles at $z/c_{ref} = 0.52$ and the appearance of reversible flow at $z/c_{ref} = 1.01$ indicate a drop in particle energy in these areas. In other words, the particles in those temporal and spatial conditions cannot re-attach the flow to the surface. Therefore, an increase in the separated bubble thickness and the expansion of the separation area occur. At $t_C = 19.5\ cs$ occur
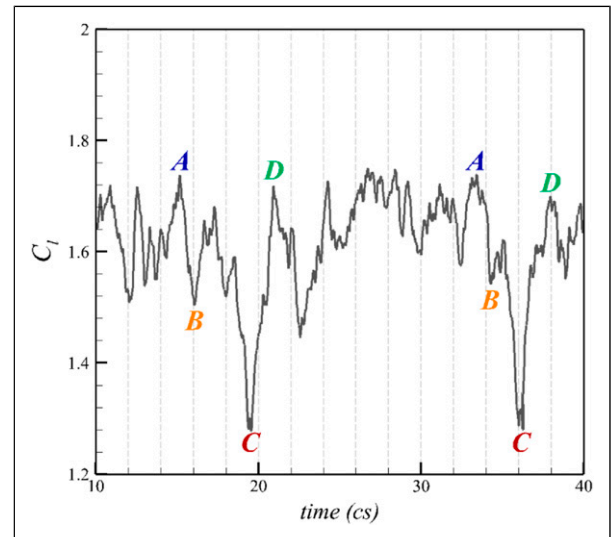
Figure 11. Time histories of the lift coefficient for Case 6 at AOA = 16°.

maximizing the bubble thickness and maximizing the separation area. These two phenomena lead to a sharp and significant drop in the lift coefficient at instant C in the most critical state. Then, with the formation of low-pressure zones in the troughs and the entry of separated flow into the upper layers, energy transfer occurs among the particles of the upper layer and the particles associated with the low-pressure zones. While recovering the energy of the particles at $t_D = 21\ cs$, the area of separated flow is reduced, and the LSBs are severely limited in terms of dimensions (thickness and length). This energy recovery, which is due to the flow momentum from the upper layers, also helps to increase the lifting force. The drop in the lift coefficient at instant D is negligible compared to the initial state and is about 1.14%. The distribution of roughness elements in the trough portions is a beneficial and efficient factor in decreasing the particle energy recovery time and laminar-to-turbulent transition process. The flow velocity around the trailing edge at the suction side was less for the uncontrolled case, whilst it increased gradually around the trailing edge when the roughness element was employed.

In order to investigate the behavior and structure of vortices on two cases 2 and 6, Fourier transforms of the vertical component of instantaneous velocity were used. This transformation is employed in two portions, $z/c_{ref} = 0.52$, 1.01 and at two points $x/c_{ref} = 0.44$, 1.03. These points are vital and practical because both represent the flow through the troughs. The flow at $x/c_{ref} = 0.44$ is located precisely behind the trough. So it is highly influenced by the patterns published by the troughs. The flow at $x/c_{ref} = 1.03$ not only reveals the behavior of the flow in the troughs section but is also representative to illustrate the interaction and development of the vortices formed and vortex shedding. One notable point in the frequency analysis performed is the greater frequency resonance in smooth and roughened cases near troughs. This event originates from flow instability, lack of eddies development with relatively strong cores, the onset of
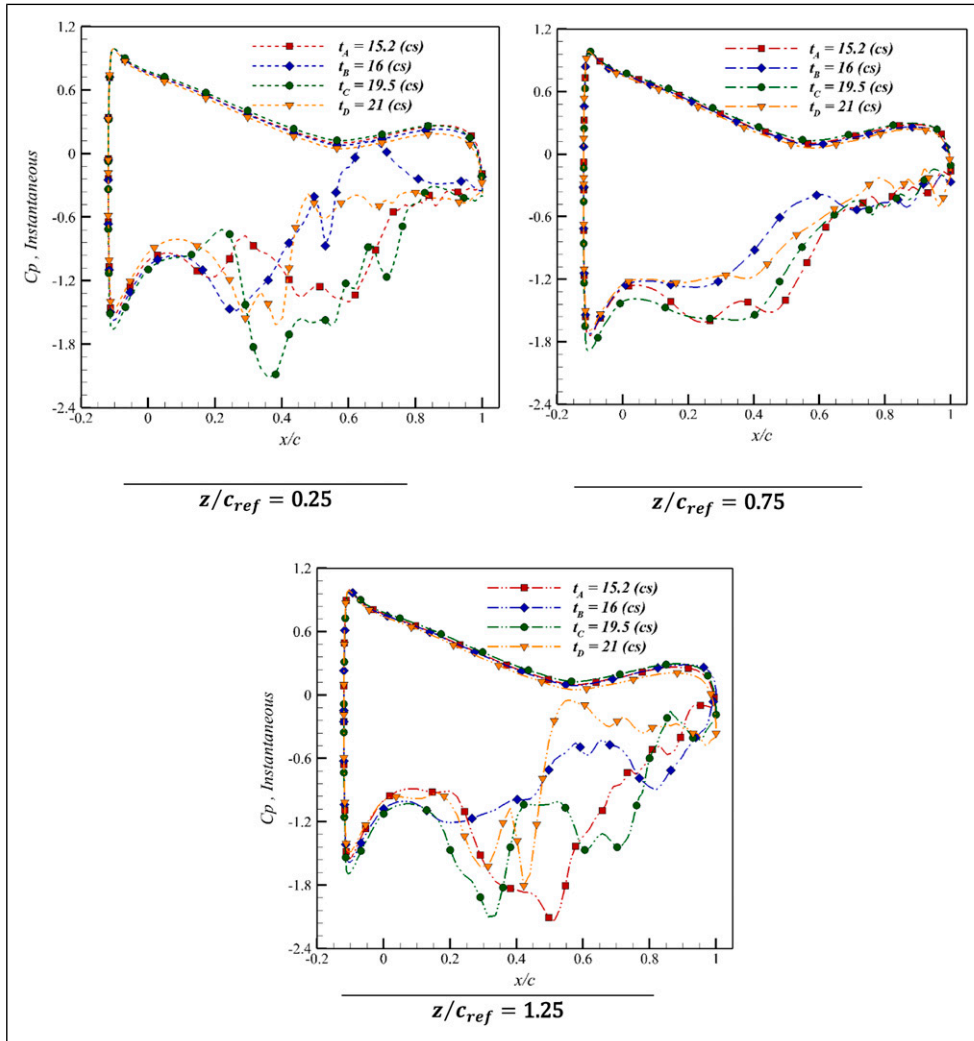
Figure 12. Instantaneous pressure coefficient along the chord of the full-span wing for Case 6 at AOA = 16°.
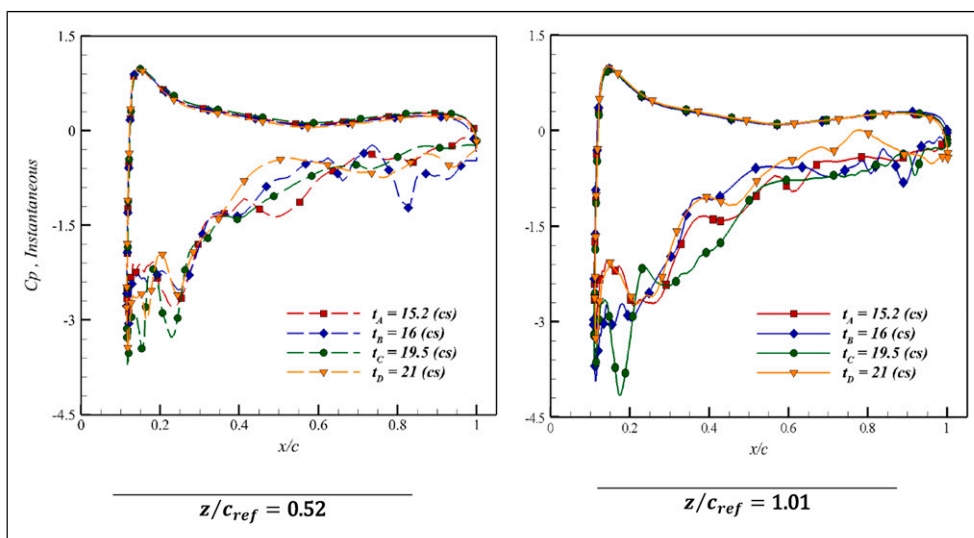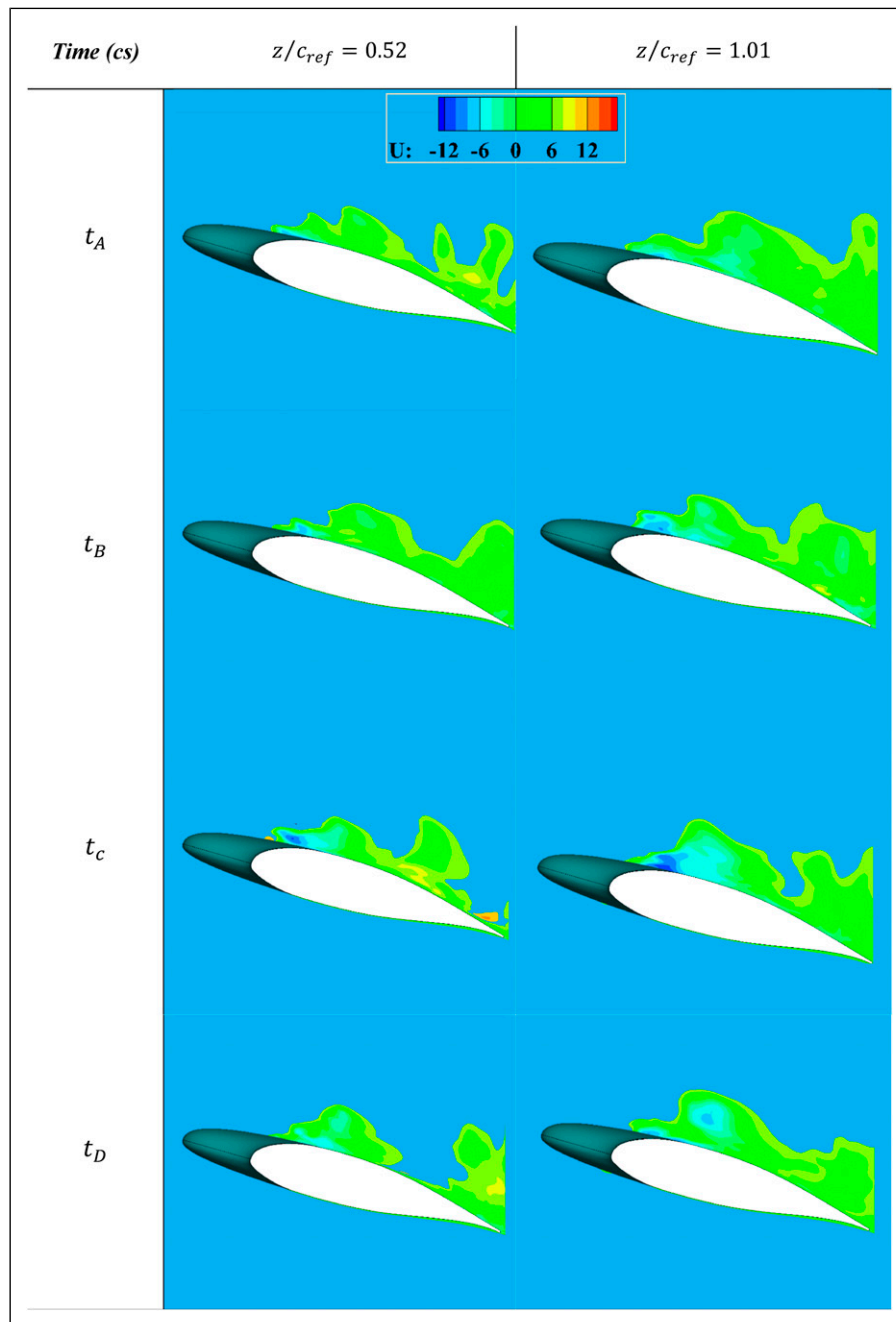

Figure 13. Instantaneous pressure coefficient along the chord of the full-span wing for Case 6 at AOA = 16°.

Figure 14. Comparison of streamwise instantaneous velocity contours on troughs ($z/c_{ref} = 0.52$, 1.01) for Case 6 at AOA = 16°.

separation, and reversible flows. In Figure 15, when the roughness height was raised, the flow fluctuations at the airfoil's trailing edge increased further. It is worth mentioning that the magnitude of the resonance frequency related to roughened aerofoil at $x/c_{ref} = (0.44, 1.03)$ and $z/c_{ref} = (0.52, 1.01)$ coordinates is 19.41, 1.60, 13.38, and 9.36 Hz, respectively, in four cases. They are much greater than the frequency of smooth aerofoil. Indeed, in roughened cases, a local interaction between them has strengthened the vortices' core while forming vortices due to roughness. Another noteworthy point is that the vortices are smaller and, at the same time, their frequency is higher in Case 6 than in Case 2, which is published streamwise.

The influence of the incidence angles

Obviously, by reducing the AOA, the size of the separation areas and the dimensions of the LSB gradually decline. To investigate the effect of altering the AOA on the arrangement and behavior of the flow, each of the leading-edge protuberances of the base model (Case 2) and modified model (Case 6) were simulated at $AOA = 8$ and 12 degrees. The findings demonstrate that the changes made by the roughness elements are positive. According to Table 1, 38% and 45% improvement in the ratio of lift-to-drag can be claimed at angles 8 and 12, respectively. In $AOA = 8°$, due to the reduction of volume and
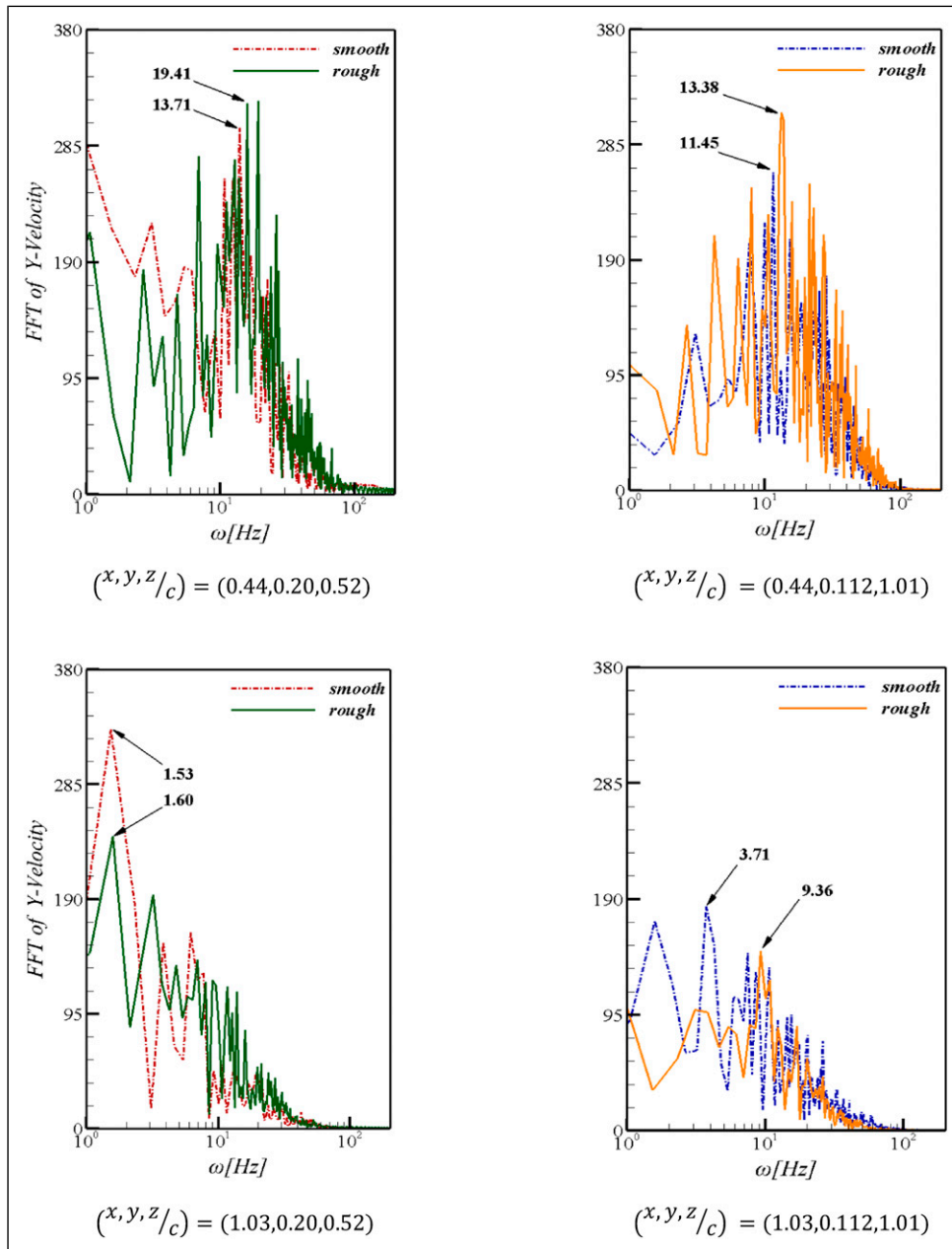
Figure 15. Fast Fourier transform vertical component of the instantaneous velocity of flow around two points $x/c_{ref} = (0.44, 1.03)$ in two portions of the trough with characteristic $z/c_{ref} = (0.52, 1.01)$ for Case 6 at AOA = 16°.

Table 2. Influence of varying the AOA on the rate of lift-to-drag coefficient for two cases 2 and 6 and comparing the corresponding improvement percentage.

c_l/c_d			
AOA (degree)	Smooth	Roughened	Percentage of improvement (%)
8	6.68	9.22	~38
12	6.54	9.5	~45

AOA: angle of attack.

dimensions of the separation bubble, the roughness impact has been reduced. In contrast, at the $AOA = 12°$, significant aerodynamic improvements have been achieved (Table 2).

Also, to complete the previous section, it is possible to acknowledge the structure and flow pattern changes in each condition without and with roughness. For this purpose, in Figure 16, iOS-surfaces
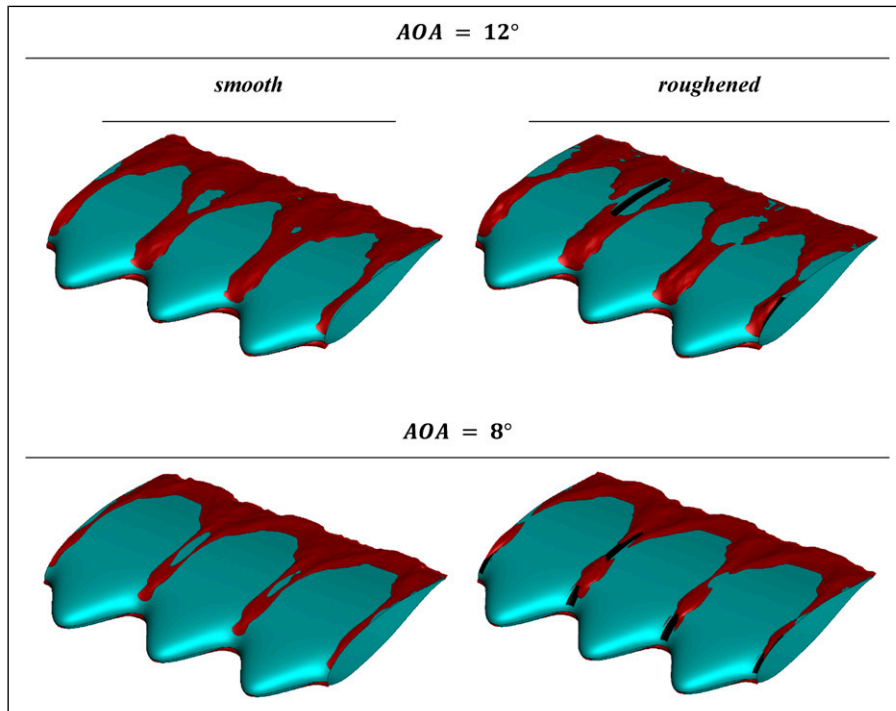
Figure 16. Time-averaged ISO-surface $V_x = 0$ related to the influence of varying the angle of attack on each of Cases 2 and 6.

related to time-average velocity (with characteristic $V_x = 0$) are presented for Cases 2 and 6 at $AOA = 8$ and 12°. As mentioned earlier, the roughness elements had a positive influence on the flow pattern and behavior. They took a practical step towards improving the performance of sinusoidal aerofoils in pre-stall situations.

Conclusions

The motivation behind this study was to improve the efficiency of MAVs with fixed wings that can operate at low Reynolds numbers due to their small size. From the design point of view, it is not reasonable to scale down versions of larger aircraft because keeping all the characteristics of conventional aircraft in a small size enhances the complexity. Hence, the miniaturization progress of MAVs has practically stopped due to various physical and technological challenges. The most prevalent issues are generating a sufficient high lift-to-drag ratio at low Reynolds numbers, expanding the payload capacity, and increasing endurance and flight range in most missions of such vehicles. In this section, the main findings of the work are summarized:

1. The flow passing on leading-edge protuberances due to deflection of the continuous current that originates from the peaks to the troughs can cause a noticeable pressure drop at the downstream region of the troughs.
2. The lift characteristics of infinite leading-edge tubercles wings were negatively affected at pre-stall conditions due to the establishment of long separation bubbles in the regions immediately downstream of the troughs. A

clear signature of streamwise vortices emanating from the vicinity of the troughs was also detected at these moderate incidences, thereby disclosing the principal mechanism behind the passive stall control technique.
3. Velocity distribution demonstrated that flow recuperation was obtained with an increment of velocity and decreased pressure via the roughness element at the airfoil suction side. Thus, the aerodynamic lift force was significantly increased.
4. According to previous research, static roughness elements are beneficial only if they settle in the proper dimensions and position (Cases 4 and 6 in the present study). Otherwise, increased frictional drag will reduce aerodynamic performance (Cases 3 and 5 in the present study).
5. The lift coefficient of Case 2 reduced by about 19.78% compared to Case 1, while its drag coefficient increased by about 3%. As revealed in data, the lift coefficient of Case 3 and Case 5 augmented by 1.37% and 3.23% compared to Case 2, respectively. Additionally, such an arrangement of roughness elements increases frictional drag. Therefore, the drag coefficients of Case 3 and Case 5 are ~5.4% lower than that of Case 2. Alternatively, if the position and dimensions of static roughness elements are appropriate, then aerodynamic performance can be improved. In addition to increasing the lift coefficient in these models (approximately 7.94% and 15.65% compared to Case 2, respectively), the drag coefficient has also reduced by around 4.6% compared to Case 2.
6. The optimal arrangement of static roughness elements can accelerate the laminar-to-turbulent transition process and efficiently reduce the stresses caused by the reversible and separation flows (such as Case 6 in the current study).

7. Roughness decreases the size of the vortices and strengthens the cores associated with them. This claim can be interpreted with frequency analysis. In a way, the static roughness elements step toward reducing and limiting the rotation of the flow.

8. Although the flow arrangement is unique at each AOA, it can be effective in other angles as well if the arrangement of the roughness elements at one angle is appropriate. This event occurred in the present study at 16, 12, and 8-degree angles.

Flow in the boundary layer had sufficient momentum to overcome the adverse pressure gradient with occurring bypass transition and keep the flow in its direction via the roughness element. Besides, both aerodynamic lift forces at lower angles of attack were increased. Static roughness elements could effectively control flow separation and formation of LSB. Consequently, it could be said that it was an effective, practical, and cheaper solution to increase the aerodynamic MAVs performance and energy efficiency.[40]

Declaration of conflicting interests

Funding

ORCID iD

Mohammad Hassan Djavareshkian ⓘ https://orcid.org/0000-0003-1766-1190

References

1. Fish FE and Battle JM. Hydrodynamic design of the humpback whale flipper. *J Morphol* 1995; 225: 51–60.
2. Abbott IH and Von Doenhoff AE. *Theory of wing sections: including a summary of airfoil data*. New York: Courier Corporation, 2012.
3. Fish FE, Weber PW, Murray MM, et al. *The Tubercles on Humpback Whales' flippers: application of bio-inspired technology*. England: Oxford University Press, 2011.
4. Miklosovic DS, Murray MM, Howle LE, et al. Leading-edge tubercles delay stall on humpback whale (Megaptera novaeangliae) flippers. *Phys Fluids* 2004; 16: L39–L42.
5. Miklosovic DS, Murray MM and Howle LE. Experimental evaluation of sinusoidal leading edges. *J Aircraft* 2007; 44: 1404–1408.
6. Weber PW, Howle LE, Murray MM, et al. Computational evaluation of the performance of lifting surfaces with leading-edge protuberances. *J Aircraft* 2011; 48: 591–600.
7. Van Nierop EA, Alben S and Brenner MP. How bumps on whale flippers delay stall: an aerodynamic model. *Phys Rev Lett* 2008; 100: 054502.
8. Stein B and Murray M. Stall mechanism analysis of humpback whale flipper models. *Proc Unmanned Untethered Submersible Technology (UUST), UUST05* 2005; 5: 21–24 August.
9. Zhang MM, Wang GF and Xu JZ. Experimental study of flow separation control on a low-Re airfoil using leading-edge protuberance method. *Exp Fluids* 2014; 55: 1710.
10. Johari H, Henoch C, Custodio D, et al. Effects of leading-edge protuberances on airfoil performance. *AIAA Journal* 2007; 45: 2634–2642.
11. Hansen KL, Kelso RM and Dally BB. Performance variations of leading-edge tubercles for distinct airfoil profiles. *AIAA Journal* 2011; 49: 185–194. DOI: 10.2514/1.J050631.
12. Bolzon MD, Kelso RM and Arjomandi M. Tubercles and their applications. *J Aerosp Eng* 2016; 29: 04015013.
13. Serson D, Meneghini JR and Sherwin SJ. Direct numerical simulations of the flow around wings with spanwise waviness. *J Fluid Mech* 2017; 826: 714–731.
14. Cai C, Zuo Z, Liu S, et al. Numerical investigations of hydrodynamic performance of hydrofoils with leading-edge protuberances. *Adv Mech Eng* 2015; 7: 1–11.
15. Dropkin A, Custodio D, Henoch CW, et al. Computation of flow field around an airfoil with leading-edge protuberances. *J Aircraft* 2012; 49: 1345–1355.
16. Melo De Sousa J and Camara J. Numerical study on the use of a sinusoidal leading edge for passive stall control at low Reynolds number. In: *51st AIAA Aerospace Sciences Meeting including the New Horizons Forum and Aerospace Exposition*, Grapevina, TX, 7-10 January, Texas, 2013.
17. Pendar M-R, Esmaeilifar E and Roohi E. LES study of unsteady cavitation characteristics of a 3-D hydrofoil with wavy leading edge. *Int J Multiphase Flow* 2020; 132: 103415.
18. Zhao M, Zhang M and Xu J. Numerical simulation of flow characteristics behind the aerodynamic performances on an airfoil with leading edge protuberances. *Eng Appl Comput Fluid Mech* 2017; 11: 193–209.
19. Custodio DS. *The effect of Humpback Whale-like protuberances on hydrofoil performance*. United States: Worcester Polytechnic Institute MA, 2007.
20. Mattos BD, Meneghini J, Padilha BR, et al. The airfoil thickness effect on wavy leading edge performance. In: *54th AIAA Aerospace Sciences Meeting*, San Diego, California, USA, 4–8 January 2016, 2016.
21. Wei Z, New TH and Cui YD. An experimental study on flow separation control of hydrofoils with leading-edge tubercles at low Reynolds number. *Ocean Eng* 2015; 108: 336–349.
22. Zhang MM, Wang GF and Xu JZ. Aerodynamic control of low-Reynolds-number airfoil with leading-edge protuberances. *AIAA Journal* 2013; 51: 1960–1971.
23. Zhang MM, Wang GF and Xu JZ. Effect of Humpback Whale-like leading-edge protuberances on the low Reynolds number airfoil aerodynamics. *Fluid-structure-sound interactions and control*. United States: Springer, 2014, pp. 107–113.
24. Mehraban A, Djavareshkian MH, Sayegh Y, et al. Effects of smart flap on aerodynamic performance of sinusoidal leading-edge wings at low Reynolds numbers. *Proc Inst Mech Eng Part G: J Aerospace Eng* 2020; 235: 439–450.
25. Mehraban A and Djavareshkian M. Experimental investigation of ground effects on aerodynamics of sinusoidal leading-edge wings. *Proc Inst Mech Eng Part C: J Mech Eng Sci* 2020; 234: 1–14, doi:10.1177/0954406220975422, https://doi.org/10.1177/0954406220975422.
26. Cai C, Zuo Z, Maeda T, et al. Periodic and aperiodic flow patterns around an airfoil with leading-edge protuberances. *Phys Fluids* 2017; 29: 115110.
27. Hansen KL, Rostamzadeh N, Kelso RM, et al. Evolution of the streamwise vortices generated between leading edge tubercles. *J Fluid Mech* 2016; 788: 730–766.

28. Rostamzadeh N, Hansen KL, Kelso RM, et al. The formation mechanism and impact of streamwise vortices on NACA 0021 airfoil's performance with undulating leading edge modification. *Phys Fluids* 2014; 26: 107101.

29. Sreejith B and Sathyabhama A. Experimental and numerical study of laminar separation bubble formation on low Reynolds number airfoil with leading-edge tubercles. *J Braz Soc Mech Sci Eng* 2020; 42: 1–15.

30. Pérez-Torró R and Kim JW. A large-eddy simulation on a deep-stalled aerofoil with a wavy leading edge. *J Fluid Mech* 2017; 813: 23–52.

31. Skillen A, Revell A, Pinelli A, et al. Flow over a wing with leading-edge undulations. *Aiaa J* 2015; 53: 464–472.

32. Esmaeili A, Delgado HEC and Sousa JMM. Numerical simulations of low-Reynolds-number flow past finite wings with leading-edge protuberances. *J Aircraft* 2018; 55: 226–238. DOI: 10.2514/1.C034591.

33. Esmaeili A and Sousa J. Influence of wing aspect ratio on passive stall control at low Reynolds number using sinusoidal leading edges. In: 29th Conference of the International Council of the Aeronautical Sciences, St Petersburg, Russia, 7–12 September 2014, 2014.

34. Rostamzadeh N, Kelso RM and Dally B. A numerical investigation into the effects of Reynolds number on the flow mechanism induced by a tubercled leading edge. *Theor Comput Fluid Dyn* 2017; 31: 1–32. DOI: 10.1007/s00162-016-0393-x.

35. Jung YS and Baeder J. Simulations for effect of surface roughness on wind turbine aerodynamic performance. *J Phys Conf Ser* 2020; 1452: 012055.

36. Liu Y, Li J and Smits AJ. Roughness effects in laminar channel flow. *J Fluid Mech* 2019; 876: 1129–1145.

37. Shrestha P and Candler GV. Direct numerical simulation of high-speed transition due to roughness elements. *J Fluid Mech* 2019; 868: 762–788.

38. Wu W and Piomelli U. Effects of surface roughness on a separating turbulent boundary layer. *J Fluid Mech* 2018; 841: 552–580.

39. Stripf M, Schulz A and Wittig S. Surface roughness effects on external heat transfer of a HP turbine vane. *J Turbomach* 2005; 127: 200–208.

40. Serdar GENÇ M, Koca K and Açikel HH. Investigation of pre-stall flow control on wind turbine blade airfoil using roughness element. *Energy* 2019; 176: 320–334.

41. Langtry R and Menter F. *Overview of industrial transition modelling in CFX*. Germany: ANSYS Germany GmbH, ANSYS CFX, 2006.

42. Pereira JCF and Sousa JMM. Finite volume calculations of self-sustained oscillations in a grooved channel. *J Comput Phys* 1993; 106: 19–29.

43. Menter FR, Langtry RB, Likki S, et al. *A correlation-based transition model using local variables—part I: model formulation*. 3rd ed. journal of Turbomachinery, 2006, 128, pp. 413–422.

44. Spalart PR and Streett C. *Young-person's guide to detached-Eddy simulation grids*. Boeing Commercial Airplane Group Seattle, WA United States: NASA/CR-2001-211032, 2001.

45. Seddon J and Goldsmith EL. Intake aerodynamics - second edition. *Aircraft Eng Aerospace Technology* 2000; 72: 1, doi: 10.1108/aeat.2000.12772aae.001.

46. Shur ML, Spalart PR, Strelets MK, et al. A hybrid RANS-LES approach with delayed-DES and wall-modelled LES capabilities. *Int J Heat Fluid Flow* 2008; 29: 1638–1649.

47. Lei H, Zhou D, Bao Y, et al. Three-dimensional improved delayed detached Eddy simulation of a two-bladed vertical axis wind turbine. *Energy Convers Management* 2017; 133: 235–248.

48. Saini R, Karimi N, Duan L, et al. Effects of near wall modeling in the improved-delayed-detached-eddy-simulation (IDDES) methodology. *Entropy* 2018; 20: 771.

49. Kobayashi MH, Pereira JCF and Sousa JMM. Comparison of several open boundary numerical treatments for laminar recirculating flows. *Int J Numer Meth Fluids* 1993; 16: 403–419.

50. Sousa JMM and Silva LMG. Transition prediction in infinite swept wings using Navier-Stokes computations and linear stability theory. *Comput Structures* 2004; 82: 1551–1560.

51. Hansen K, Kelso R and Dally B. An investigation of three-dimensional effects on the performance of tubercles at low Reynolds numbers. In: 17th Australasian Fluid Mechanics Conference. Auckland: New Zealand, 5–9 December 2010, 2010.

52. Xingwei Z, Chaoying Z, Tao Z, et al. Numerical study on effect of leading-edge tubercles. *Aircraft Eng Aerospace Technology* 2013; 85: 247–257.

53. Anderson JD, Jr. *Fundamentals of Aerodynamics*. New York: Tata McGraw-Hill Education, 2010.

54. Wokoeck R, Krimmelbein N, Ortmanns J, et al. RANS simulation and experiments on the stall behaviour of an airfoil with laminar separation bubbles. In: 44th AIAA Aerospace Sciences Meeting and Exhibit, 9-12 Janurary, Ren, Nevada United States, 2006.

55. Chen J-H. The effect of humpback whale-like leading edge protuberances on hydrofoil performance. In: 15th International Symposium on Flow Visualization, June, 25-28, 2012.

Appendix

Notation

c	Chord length
C_l	Lift coefficient
C_d	Drag coefficient
C_P	Pressure Coefficient
h_R	Roughness height
I_R	Roughness length
R_e	Reynolds number
U_∞	Velocity of potential flow
w_R	Roughness width
α	Angle of Attack
ρ	Air density
ν	Velocity

Subscripts

L	Lift
D	Drag
p	Pressure
max	Maximum
f	Fraction

Abbreviation

LSB	Laminar separation bubble
CFD	Computational fluid dynamics
AOA	Angle of attack
2D	Two dimensional
SST	Sheer stress transport